INORGANIC CHEMISTRY FRONTIERS

RESEARCH ARTICLE

View Article Online
View Journal | View Issue

Check for updates

Cite this: *Inorg. Chem. Front.*, 2024, **11**, 1123

Introducing alkyl chains to realize the construction of superhydrophobic/superoleophilic MOFs and the transformation from three-dimensional to two-dimensional structure†

Xinglei He, Chunlong Yu, Jingheng Li, Zhihua Wang and Ke-Yin Ye *

Superhydrophobic metal–organic frameworks (MOFs) exhibit excellent application prospects in many fields, such as catalysis, water pollution treatment, self-cleaning, and so on. In this study, two stable salen-based three-dimensional (3D) MOFs, *i.e.*, $([Cd(CuL^s)(L)]_n$ (**1**) and $[Zn(CuL^s)(L)DMF]_n$ (**2**) [L^s = *N*,*N*′-bis(3-*tert*-butyl-5-(4-pyridyl)salicylidene)-1,2-cyclohexanediamine copper^{II}, L = [1,1′-biphenyl]-4,4′-dicarboxylic acid]), have been synthesized. To build superhydrophobic MOFs, the low-surface-energy alkyl chains were introduced, and the water contact angles (WCAs) gradually increased from 136.9° to 155.0°. Interestingly, the structures are different from **1** when the alkyl chains are *n*-butyl, *n*-hexyl, or *n*-octyl. In particular, the 3D structure changes to the 2D structure by introducing the *n*-octyl, and the 2D stacking mode with a large number of aromatic rings is also conducive to improving hydrophobicity. As evidenced by scanning electron microscopy (SEM), the introduction of alkyl chains also enhances the overall roughness of MOFs, which is also pivotal to improving hydrophobicity. In addition, the superhydrophobic/superoleophilic **1-Oct** was loaded into a sponge to achieve selective oil–water separation. Another application of this MOF-functionalized sponge was the highly selective separation of water-in-oil emulsions. It was found that the pore environment of **1-Et** was improved with the introduction of the ethyl side chain, which forms the basis for the other potential applications.

Received 1st November 2023,
Accepted 28th December 2023

DOI: 10.1039/d3qi02250a

rsc.li/frontiers-inorganic

Published on 29 Desemba 2023. Downloaded on 24/08/2025 07:02:05.

Introduction

At present, the problem of environmental pollution, especially water pollution, has been paid great attention all over the world. Frequent oil spills have seriously endangered the ecological balance and human health.[1–3] Therefore, the separation of oily wastewater with high efficiency and high selectivity is an urgent scientific problem. Hydrophobic materials, such as hydrophobic sponges,[4] hydrophobic films,[5] and aerogels,[6] have become ideal materials for oil–water separation based on the immiscibility of oil and water. One of the most important factors affecting oil–water separation performance is hydrophobicity. When the water contact angle (WCA) between the material surface and water is greater than 90°, it is defined as a hydrophobic material. When the WCA is greater than 150°, it is considered a superhydrophobic material.[7] At this point, the water droplets partially stay on the air cushion so the adhesion is low. In general, the surface roughness and surface energy determine the wettability of materials. For instance, high surface roughness and low surface energy typically lead to strong hydrophobicity.[8] How to construct highly hydrophobic materials is the key to achieving efficient oil–water separation.

Metal–organic frameworks (MOFs) are porous materials assembled by metal clusters/ions and multi-dentate organic ligands through metal–ligand coordination bonds.[9–14] MOF, knowledge of the large specific surface area and high porosity, has been successfully applied in the field of adsorption and separation.[15,16] Some hydrophobic MOFs have a good application prospect in the field of oil spill cleaning and oil–water emulsion separation.[17–23] Specifically, the excellent designability of linkers and modifiability of MOFs greatly improve the possibility of accurate construction of superhydrophobic MOFs.[24,25]

Introducing low-surface-energy fluorine elements or fluorine-containing groups into MOFs is one of the common ways to construct hydrophobic MOFs. Liu *et al.*[26] used the simple condensation reaction to graft 2,3,4,5,6-pentafluorobenzylamine onto MOF to obtain superhydrophobic ZIF-90 composites. The post-modification of ZIF-90 not only increased WCA

Key Laboratory of Molecule Synthesis and Function Discovery (Fujian Province University), College of Chemistry, Fuzhou University, Fuzhou 350108, China. E-mail: kyye@fzu.edu.cn

†Electronic supplementary information (ESI) available: Experimental section and date analysis. See DOI: https://doi.org/10.1039/d3qi02250a

Published on 29 Desemba 2023. Downloaded on 24/08/2025 07:02:05.

from 93.91° to 152.41° but also maintained a dodecahedral shape and SOD topology structure. Superhydrophobic ZIF-90 showed good absorption and separation performance for biological alcohols in water, and more than 98% of biological alcohols (ethanol, isopropanol, and butanol) could be effectively recovered at 20 °C. However, fluorine is not recommended to be widely used because of its high toxicity and high synthesis cost.[6] The modification of the alkyl chain not only does little harm to the environment but also has a low cost. In addition, the degree of hydrophobicity can be adjusted according to the length of the alkyl chain. Zhu *et al.*[27] obtained hydrophobic or even superhydrophobic UiO-67 by introducing alkyl chains of different lengths. With the length of the alkyl chain increasing, the WCAs increased from 0.0° to 154.0°. The saturated toluene aqueous solution was used to verify the oil–water separation ability of the MOFs. The result showed that the oil–water separation efficiency of alkyl chain-modified UiO-67 was up to 97%. In addition, most two-dimensional (2D) MOFs also show good hydrophobicity due to the π–π stacking between layers.

Nevertheless, in the application of oil–water separation, MOF powder still has some potential problems, such as low plasticity, poor recyclability, poor mechanical properties, and so on.[28] Commercial porous materials, such as polyurethane (PU) sponge and melamine sponge (MS), are often used as 3D porous substrates to prepare oil-absorbing materials because of their low cost, low density, high porosity, excellent mechanical properties, and simple modification.[28] However, the fixation of MOFs on porous substrates by *in situ* growth is mostly unstable, so the use of binders is a more universal method to obtain stable superhydrophobic MOF/substrate composites. Ghosh *et al.*[29] synthesized hydrophobic 1′@CF_3 by grafting CF_3 group on MOF. The stable hydrophobic 1′@CF_3@melamine was prepared by fixing 1′@CF_3 on MS with the PDMA-*co*-PMHS polymer coating. 1′@CF_3@melamine can separate oil–water mixtures and water-in-oil emulsions even in harsh water environments. The absorption capacity and separation efficiency of 1′@CF_3@melamine for various oils were 27–47 g g^{-1} and 95.99%, respectively. The combination of hydrophobic binder and hydrophobic MOF can not only improve the stability and mechanical properties of the composites but also their superposition effect is more conducive to enhancing the hydrophobicity.

In this work, two novel MOFs **1** and **2** with the same topology were obtained by the solvothermal method. Both MOFs have a rare 8-fold interpenetrating structure along the *b*-axis, which leads to their excellent stability and hydrophobicity. The initial WCAs of **1** and **2** were 136.9° and 136.4°, respectively. To regulate the wettability, the different functional groups were introduced into the carboxylic acid ligand to obtain a series of **1-R**s (R = NH_2, ethyl, *n*-butyl, *n*-hexyl, or *n*-octyl). Interestingly, when –NH_2 or ethyl were introduced, **1-NH_2** and **1-Et** isomorphic to **1** were obtained. When the length of the alkyl chain continues to increase, the crystal structure changes. In particular, the change of MOF from 3D to 2D structure has been observed through single-crystal X-ray diffraction (SC-XRD) after introducing *n*-octyl. As expected, the hydrophobicity was enhanced with the increase of low-surface-energy alkyl chains of different lengths, but **1-NH_2** became superhydrophilic. Therefore, it was concluded that the effect of functional groups on wettability is greater than interpenetration or π–π stacking between layers.

The superhydrophobic **1-Oct** is an ideal material to investigate the oil–water separation. The fixation of **1-Oct** by hydrophobic polydimethylsiloxane (PDMS) on the MS resulted in a superhydrophobic sponge (PDMS/**1-Oct**@MS) with much higher hydrophobicity than PDMS/MS (only PDMS was deposited on MS) and **1-Oct**@MS (only **1-Oct** was loaded into MS) and achieved excellent performance on the selective oil–water separation (Scheme 1). The pure oil phase could also be obtained from water-in-oil emulsions which are typically difficult to separate. When ethyl is introduced into MOF, the

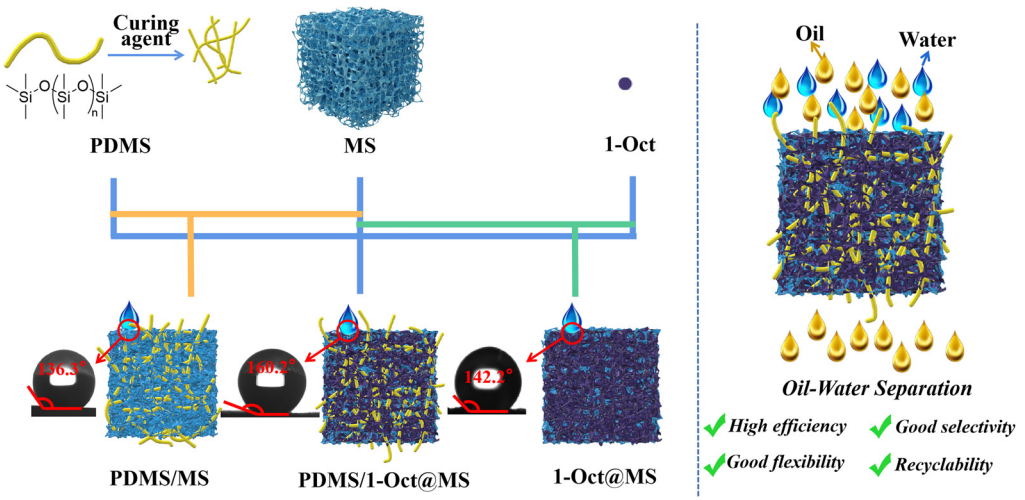

Scheme 1 Schematic diagram of preparing superhydrophobic PDMS/**1-Oct**@MS and applications in oil–water separation.

 This journal is © the Partner Organisations 2024

Published on 29 Desemba 2023. Downloaded on 24/08/2025 07:02:05.

pore environment of **1-Et** changes, the specific surface area increases greatly, and the micropore environment is produced. We speculate that the introduction of ethyl may reduce the degree of interpenetration. Overall, the introduction of the alkyl chain of appropriate length not only regulates the hydrophobicity but also changes the pore environment to enhance MOF potential in many fields (such as adsorption separation, catalysis, energy storage, *etc.*). Through this molecular coordination engineering, multi-functional hydrophobic MOFs can be easily constructed without complex hydrophobic post-modification.

Results and discussion

Materials characterization and analysis

1 and **2** were obtained by self-assembly of $Cd(NO_3)_2{\cdot}4H_2O$ or $Zn(NO_3)_2{\cdot}6H_2O$, CuL^s (*N*,*N*′-bis(3-tertbutyl-5-(4-pyridyl)salicylidene)-1,2-cyclohexanediamine copper^{II}), and H_2L ([1,1′-biphenyl]-4,4′-dicarboxylic acid) ligands (Fig. 1a). They crystallized in the *orthogonal* system with space group *Pbca* system. The asymmetric unit of **1** contained one Cd^{2+} ion, one L^{2-} ligand, and one CuL^s ligand (Fig. S1a†). Each Cd^{2+} ion formed six coordination with four oxygen atoms from two L^{2-} ligands and two N atoms from two CuL^s ligands. Slightly different from **1**, the asymmetric unit of **2** contained one Zn^{2+} ion, one L^{2-} ligand, and one CuL^s ligand (Fig. S1b†). Each Zn^{2+} ion formed four coordination with two oxygen atoms from two L^{2-} ligands and two N atoms from two CuL^s ligands. CuL^s and L^{2-} ligands acted as linear bridges to connect adjacent Cd^{2+} ions, which formed a diamond-like network (Fig. 1b) and further extension of the network formed the 3D frameworks with *dia* topology (Fig. 1c). The *dia* topology makes MOFs easy to form multiple-fold interpenetration and such an interpenetration between construction units usually increases structural stability while reduces the porosity and specific surface area.[30,31] Taking **1** for example, the non-interpenetrating network had extra-large channels, size up to 27.0 × 47.5 Å^2 along the crystallographic *c*-axis (Fig. 1d) and such a large cavity resulted in a rare 8-fold interpenetrating framework along the *b*-axis (Fig. 1e). **2** also adopted the same growth mode to form the 8-fold interpenetration. The rare interpenetrating network also led to extremely low specific surface area and almost non-existent connected pores of **1** and **2**. The effective free voids of **1** and **2** accounted for 16.5% and 16.1% of the crystal volume calculated by the PLATON analysis, respectively.[32] It could be seen from the N_2 adsorption–desorption isotherms (Fig. S2†) that both **1** and **2** exhibited type-II isotherms with an H4-type hysteresis loop. The result was in agreement with the close-packing crystallographic nature (no microporous sorption). The Brunauer–Emmett–Teller (BET) surface area (94.812 and 23.154 m^2 g^{-1}, respectively, Table S2†) should be attributed to the slit-like mesoporous formed by the aggregation of crystals.[33] It was hypothesized the highly interpenetrating structure and the existence of high-density aromatic rings make these MOFs hydrophobic.

The phase purities of **1** and **2** were established by comparing the observed and simulated PXRD patterns. The testing results suggested high phase purity and crystallinity of **1** and **2** (Fig. S3a†). In most practical applications, materials need to be exposed to different organic solvents for a long time, so solvent stability is one of the most important indicators for high-performance materials. We put **1** and **2** in different solvents for 60 days to test their solvent stability. In Fig. S5a and c,† the structures of **1** and **2** were still maintained after soaking, indicating their good solvent stability. The fact that most MOFs are difficult to exist for a long time in water, especially under harsh conditions, results in their limited applications in water-rich environments. We put **1** and **2** in

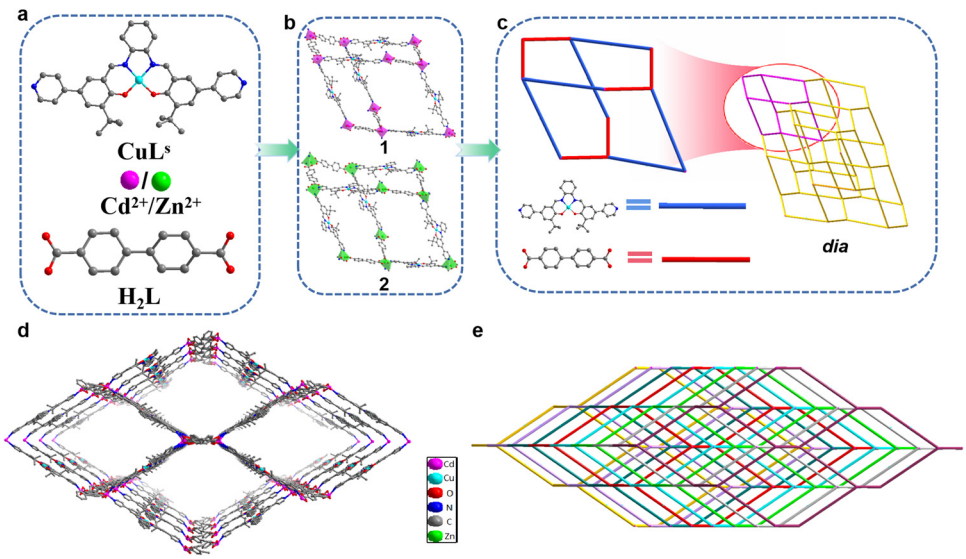

Fig. 1 Crystal structures of **1** and **2**. (a) Schematic diagram of the synthesis of **1** and **2**. (b) Diamond-like primitive networks of **1** and **2**. (c) The *dia* topology of **1** and **2** (d) no-interpenetrating 3D network with the 1D channel of **1**. (e) 8-Fold interpenetrating framework of **1** and **2**.

Published on 29 Desemba 2023. Downloaded on 24/08/2025 07:02:05.

aqueous solutions of different pH for 48 h to test their stability. The PXRD patterns of **1** (Fig. S5b†) showed excellent stability in the full range of pH. However, **2** only remained its structure intact in the pH range of 3–14 (Fig. S5d†). When pH was 1 or 2, the crystal decomposed completely and dissolved in aqueous solution. We also explored their thermal stability. It could be seen from thermogravimetry analysis (TGA) that **1** had better thermal stability than **2** (Fig. S6†). The difference in stability between **1** and **2** could be explained by the coordination structure of the metal nodes. The six-coordinated Cd atom in **1** (Fig. S7a†) is more stable than the four-coordinated Zn atom in **2** (Fig. S7b†).

1 and **2** showed hydrophobic properties due to their tightly packed aromatic rings. The static WCAs of **1** and **2** were 136.9° and 136.4° (Fig. 3a), respectively. However, most applications, such as self-cleaning, sewage treatment, waterproof coatings, medical devices, *etc.*, require the high hydrophobicity of materials. Therefore, a series of more hydrophobic or even superhydrophobic **1-R**s and **2-R**s were prepared by introducing alkyl chains of different lengths. The incorporation of those novel organic ligands into **1-R**s and **2-R**s was determined by ^{1}H NMR (Fig. S9–S12†). The thermal stabilities are also well maintained (Fig. S8†). Because **1-R**s and **2-R**s have similar properties, **1-R**s was used as the main object for further research.

PXRD further analyzed the structures of **1-R**s. Through the comparison of PXRD patterns, **1-Et** and **1** were considered to be isomorphic (Fig. S3b†) which was in line with expectations. However, when *n*-butyl, *n*-hexyl, or *n*-octyl were introduced, the PXRD patterns changed greatly (Fig. S3c and d†). We realized that the structures of **1-But**, **1-Hex**, and **1-Oct** might have changed. Through many times SC-XRD tests, only the crystal data of **1-Oct** were obtained, and the accurate structure was obtained by data refinement. The crystal data or even cell parameters of **1-But** and **1-Hex** weren't collected by SC-XRD, so it was difficult to obtain accurate structures. Therefore, the structure of **1-But** and **1-Hex** will not be discussed, but their hydrophobic properties will be briefly mentioned in this work. When *n*-octyl is introduced, **1-Oct** changes to the *triclinic* system and 2D structure (Fig. 2a). Cd^{2+} ions form a six-coordinated octahedral configuration with two N atoms from two CuL^s ligands and four O atoms from two L-Oct^{2-} ligands (Fig. 2b). The difference is that the plane angle forming by carboxyl and benzene ring in L-Oct^{2-} (49.7°, Fig. S4b†) is much larger than L^{2-} (12.5°, Fig. S4a†), which makes the repetitive unit of **1-Oct** tend to expand infinitely in 2D plane under the action of bridging ligands (Fig. 2b). By comparing with the simulated PXRD pattern, it is proved that the synthesized **1-Oct** has good crystallinity and phase purity (Fig. S3d†). As far as we know, the transition of 3D to 2D structure caused by the introduction of alkyl side chains was rarely reported, which may be a very interesting phenomenon.

A series of **1-R**s were studied to investigate the effect of functional groups on the wettability of MOFs. One drop of water or *n*-hexane was dripped on the surfaces of **1**, **1-Et**, **1-But**, **1-Hex**, or **1-Oct** powders, respectively. While the shape of the water droplets was maintained, the oil droplets were immediately completely infiltrated (Fig. 3b and Movie S1†). It also showed that these MOFs are hydrophobic and superoleophilic. Furthermore, WCAs increased gradually from 136.9° to 155.0° with the increase in the length of alkyl chains (Fig. 3a, b and d). Even when the water droplet was kept on superhydrophobic **1-Oct** powder for 30 minutes, the WCA hardly changed (Fig. S13†). This also reflected the superhydrophobic stability of **1-Oct**. When water was dropped on the ligands, including H_2L–Et, H_2L–But, H_2L–Hex, or H_2L–Oct powders, no matter how long the alkyl chain was, it could not prevent the powder from being infiltrated gradually (Fig. 3c). However, when carboxylates were regularly arranged as linkers in **1-R**s, alkyl chains would play a hydrophobic role by reducing the surface energy and/or wrapping the metal nodes and carboxylates at a molecular level.[27] When the $-NH_2$ was also introduced to **1**, the hydrophilicity of $-NH_2$ reduced the WCA of **1-NH$_2$** to 0° (Fig. S14†). It showed that the effect of functional groups was much greater than structural interpenetration or π–π stacking between layers in the wettability of MOFs.

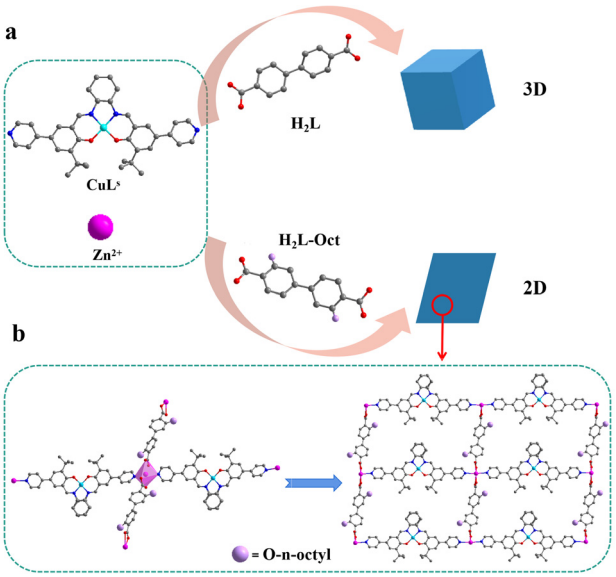

Fig. 2 (a) Diagram of synthesis and structure of **1** and **1-Oct**. (b) Coordination environment and 2D plane of **1-Oct**.

The morphology of **1-R**s was characterized to support the hydrophobic mechanism. As illustrated in Fig. 4, **1-R**s (R = NH_2, H, ethyl, *n*-butyl, *n*-hexyl, or *n*-octyl) showed irregular flakes and most of the crystals were aggregated. The crystal morphology of **1** and **1-NH$_2$** was relatively complete and large (Fig. 4a and f). With the introduction of alkyl chains, the crystals became more irregular and the crystal cracks increased gradually (Fig. 4b–e). Magnifying the **1** and **1-NH$_2$**, it could be observed that the crystal surfaces were very smooth (Fig. 4a and f). However, other crystals become rougher with the introduction of alkyl chains (Fig. 4b–e). The uneven surface could be also observed for **1-But**, **1-Hex**, and **1-Oct** (Fig. 4c–e). The introduction of alkyl chains not only reduces the surface energy of MOFs but also increases their roughness.[27] All these facts improve the hydrophobicity of MOFs. Since such a large

This journal is © the Partner Organisations 2024

Published on 29 Desemba 2023. Downloaded on 24/08/2025 07:02:05.

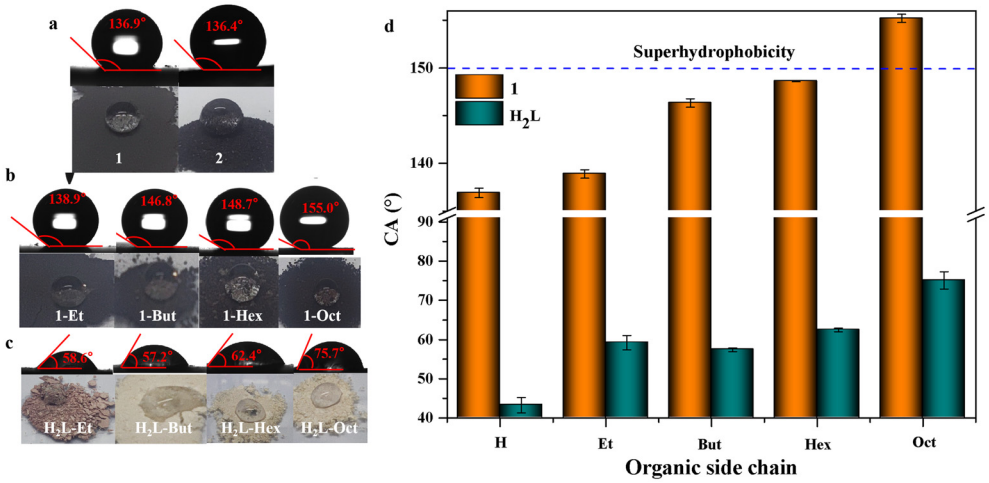

Fig. 3 Static WCAs and digital photographs of **1** and **2** (a), **1-Rs** (b), and H_2L–Rs (c). Histogram with the experimental error bars of static WCAs (taking the average of three times) of **1-Rs** and H_2L–Rs (d).

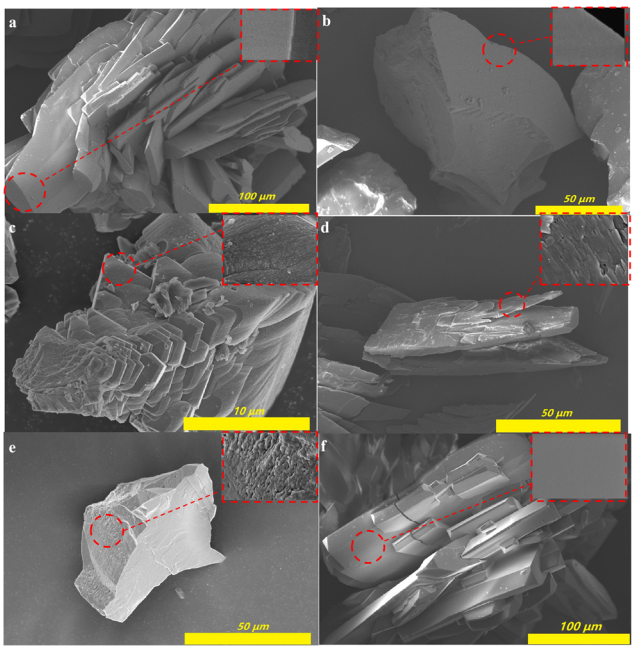

Fig. 4 The SEM images of **1** (a), **1-Et** (b), **1-But** (c), **1-Hex** (d), **1-Oct** (e), and **1-NH$_2$** (f). (The insets were magnified images of the crystal surface.)

size of MOFs is not conducive to practical application,[28,34] small size **1-Oct** powder (s**1-Oct**) was synthesized by stirring instead of the traditional solvothermal method. As expected, though the size of s**1-Oct** was smaller than **1-Otc** (Fig. S15a†), its crystal structure (Fig. S15b†) and WCA (Fig. S15a†) remained intact. This also provided the basis for the large-scale synthesis and potentially practical application of **1-Rs**.

Oil–water separation

MS is considered one of the most promising materials for oil–water separation due to its low cost, strong mechanical properties, high stability, and modifiability.[28,35,36] The hydrophobicity of materials will have a great influence on the oil–water separation ability, so **1-Oct** which has the highest hydrophobicity is chosen to modify MS for oil–water separation. The PDMS was used as the binder to fix **1-Oct** onto MS uniformly and the average load was 6.6 mg (Table S5†). By contrast, **1-Oct** was very easy to fall off without PDMS (Fig. S16b†). A large amount of powder at the bottom of the **1-Oct**@MS could also be observed in the SEM images (Fig. S16c†). In Fig. S17a, b, d, and e,† each fiber of MS or PDMS/MS was very smooth, while the fibers became rough after loading **1-Oct**, and a large number of particles were uniformly loaded on the fibers (Fig. S17c and f†). Through energy dispersive spectrometer (EDS) analysis, these rough fibers existed Cd and Cu elements (Fig. S18†) and their mass ratio conformed to the theoretical value (Table S3†). The PXRD pattern of PDMS/**1-Oct**@MS showed an obvious characteristic peak of **1-Oct** at 6.9°, which proved that **1-Oct** was uniformly loaded on MS (Fig. S19a†). FTIR spectra further demonstrated the successful preparation of PDMS/**1-Oct**@MS. The spectra of PDMS/**1-Oct**@MS displayed the characteristic absorption peak of **1-Oct** at 1589 cm^{-1} (Fig. S19b†), demonstrating that **1-Oct** was successfully loaded. The peaks at 788 cm^{-1}, 1009 cm^{-1}, 1256 cm^{-1}, and 2958 cm^{-1} were assigned to the Si–C stretching vibration, Si–O–Si stretching vibration, Si–CH_3 stretching vibration, and C–H asymmetric stretching vibration, respectively, demonstrating that PDMS was successfully deposited (Fig. S19b†).[4] Based on these results, the hydrophobicity of PDMS/**1-Oct**@MS was studied. In Fig. 5a, water and oil drops could be completely infiltrated in MS, indicating that it was not selective. When only PDMS was loaded on MS, the material became hydrophobic and the water drop could be maintained on PDMS/MS (Fig. 5a) with the WCA of 136.3° (Fig. 5c). When PDMS was replaced by **1-Oct**, the WCA of **1-Oct**@MS was 142.2° (Fig. S16a†). After loading both **1-Oct** and PDMS, deionized water and saltwater drops could remain with the WCA of 160.2° while the oil drop completely infiltrated (Fig. 5a and d).

Published on 29 Desemba 2023. Downloaded on 24/08/2025 07:02:05.

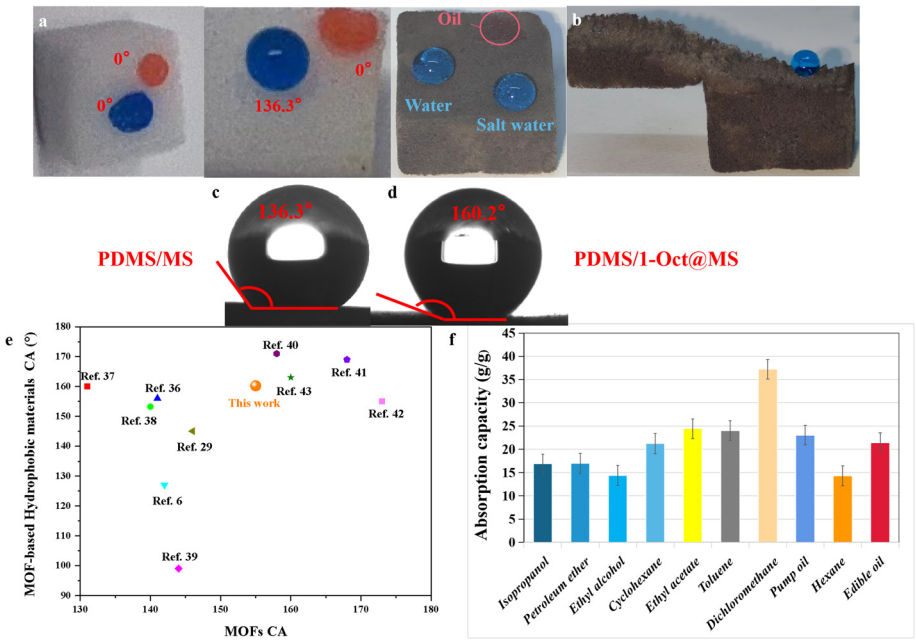

Fig. 5 (a) Digital photographs of hydrophobicity test of MS, PDMS/MS, and PDMS/**1-Oct**@MS. (b) Digital photographs of hydrophobicity test of PDMS/**1-Oct**@MS cross-section (c) the WCA of PDMS/MS. (d) The WCA of PDMS/**1-Oct**@MS. (e) The WCAs of reported MOFs and MOF-based materials. (f) Absorption capacity of PDMS/**1-Oct**@MS for different oils.

After cutting the PDMS/**1-Oct**@MS, the internal cross-section also remained hydrophobicity (Fig. 5b), suggesting the uniform loading of **1-Oct**. By loading **1-Oct** and PDMS, the originally superhydrophilic and superoleophilic sponge changed into superhydrophobic and superoleophilic functional porous materials. It can be attributed to the superposition effect of PDMS and **1-Oct**. Compared with many reported MOFs and MOF-based sponges, **1-Oct** and PDMS/**1-Oct**@MS performed better hydrophobicity (Fig. 5e).[6,29,36–43] The oil absorption capacity (Q) of PDMS/**1-Oct**@MS was determined to be 17–38 g g^{-1} (Fig. 5f). It indicates that the oil or organic solvent absorption capacity of PDMS/**1-Oct**@MS is lower than some superhydrophobic MS-based sponge or polysaccharide-based aerogel sorbent materials reported in the literature.[44–46]

PDMS/**1-Oct**@MS was then applied to oil–water separation. Excellent separation performance could be achieved for both low-density toluene (red) and water (blue) mixture and high-density dichloromethane (red) and water (blue) mixture (Fig. 6a and b, Movies S2 and S3†). Furthermore, taking dichloromethane as the object, the oil–water separation efficiency was 99.2% and the flux was 8062 L m^{-2} h^{-1} under an effective separation area for a circle with a diameter of 6 mm. The selectivity is very important for oil–water separation, so PDMS/**1-Oct**@MS was used to absorb water to verify its high selectivity. To simulate the oil–water separation application and solve the problem of poor absorption capacity, a simple and efficient continuous flow pumping device was built. The PDMS/**1-Oct**@MS was connected to the pump and put into the water (blue). Another liquid outlet was put into the colorless water. When the pump started, the liquid outlet discharged bubbles, the water was still clear and colorless, and the water level in the bottle was the same before and after the absorption process (Fig. S21†). Even if PDMS/**1-Oct**@MS was pressed into deep water, the same result was obtained (Fig. 6d, Movie S4†). However, the water level of the outlet rose and the colorless water became blue after PDMS/**1-Oct**@MS was replaced by MS (Fig. 6c, Movie S5†), which implied that PDMS/**1-Oct**@MS had excellent absorption selectivity. To simulate the actual application of oil absorption on the 'sea' surface more realistically, 'sea' water and waves were prepared by adding the right proportion of salt and constant shaking of the bottle. When the pump was started, the oil (red) was selectively and gradually pumped out of the 'sea' surface (blue) (Fig. 6e and Movie S6†).

In the presence of surfactant, the oil–water emulsion is difficult to separate directly because of its stable interfacial properties.[4] Surprisingly, PDMS/**1-Oct**@MS could effectively separate the oil–water emulsion. Specifically, after immobilizing PDMS/**1-Oct**@MS in a glass funnel, the surfactant-stabilized oil–water emulsion was poured into the funnel (Fig. 7a). Dichloromethane (red) was gradually separated under gravity (Fig. 7b and Movie S7†). The separated dichloromethane was observed to show that had almost no water droplets by an optical microscope (Fig. 7c). This further emphasized the successful separation of oil–water emulsion. In this process, the separation efficiency was 98.9% and the flux was 2389 L m^{-2} h^{-1}. Compared with some reported literature,[47–49] PDMS/**1-Oct**@MS has good separation efficiency and flux in oil–water separation and water-in-oil emulsion separation. The reusability of materials is also an important reference factor in practical applications. After completing 50 times absorption cycles in petroleum ether, the absorption capacity and WCAs only showed a slightly downward trend (Fig. 8a and b).

 This journal is © the Partner Organisations 2024

Published on 29 Desemba 2023. Downloaded on 24/08/2025 07:02:05.

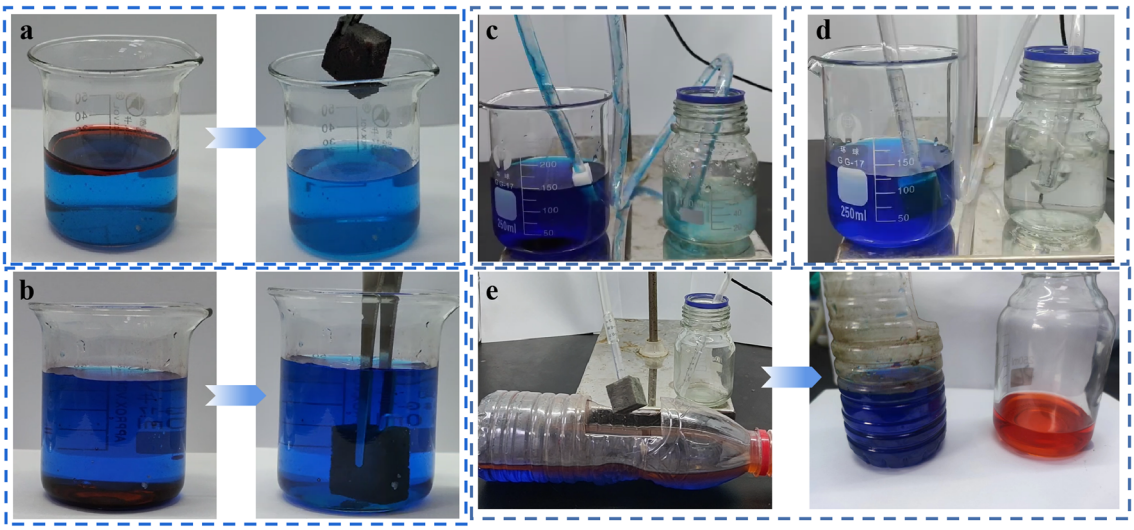

Fig. 6 Oil–water separation of low-density toluene (red) and water (blue) mixture (a) and high-density dichloromethane (red) and water (blue) mixture (b). (c) Absorption of water by untreated sponge. (d) Selective absorption of PDMS/**1-Oct**@MS in water. (e) Oil–water separation on the simulated sea surface.

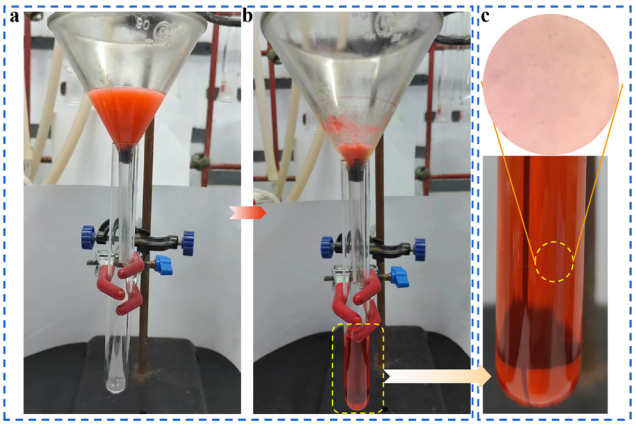

Fig. 7 (a) Separation device of water-in-oil emulsion. (b) Separation of water-in-oil emulsion under the action of gravity. (c) Image of separated dichloromethane under the optical microscope.

Meanwhile, the characteristic peak of **1-Oct** in the PXRD pattern of PDMS/**1-Oct**@MS remained intact, too (Fig. 8c). The SEM image and EDS analysis also showed that the **1-Oct** on the MS fibers maintained a uniform distribution (Fig. 8d and S20†). **1-Oct** was loaded onto MS to obtain a superhydrophobic porous sponge and achieved outstanding performance in the oil–water separation test, which was expected to be applied in practical oil–water separation.

The possible mechanism of oil–water and water-in-oil emulsion separation

Wettability may be one of the most important factors affecting the process of oil–water separation. PDMS/**1-Oct**@MS has superhydrophobicity and superoleophilicity. Therefore, when the immiscible oil–water mixture is added to the separation system, the surface of PDMS/**1-Oct**@MS will absorb oil and repel water, to achieve the purpose of oil–water separation. When the water-in-oil emulsion is added to the system, the oil spreads to the PDMS/**1-Oct**@MS actively under the action of gravity to form an oil layer. The oil is then continuously pushed into the PDMS/**1-Oct**@MS filled with the oil layer, and repels the water to achieve separation.[46]

Analysis of N_2 adsorption characteristics of 1, 1-Et, and 1-Oct

1 with 8-fold interpenetration shows the type-II adsorption–desorption isotherm, which is also consistent with the tight packing characteristics. Interestingly, when ethyl is introduced, the adsorption characteristic of **1-Et** completely changes from type-II to type-I adsorption–desorption isotherm which shows that **1-Et** has a microporous environment (Fig. S22†). The BET surface area is 189.174 $m^2\ g^{-1}$ for **1-Et**, much larger than **1**. The pore size distribution (PSD) calculated based on the Density Function Theory (DFT) method is around 0.5 nm and 1 nm (Fig. S23†), which is consistent with the conclusion of the micropore environment. The difference between the adsorption characteristics of **1** and **1-Et** may be due to the decrease of interpenetrating degree caused by the introduction of ethyl, thus forming a microporous environment. Some literature has summarized the methods to regulate the degree of interpenetration, in which it is feasible to change the size of the ligand.[50–53] The degree of interpenetration can affect the physical properties of materials, such as pore size, porosity, thermodynamic stability, flexibility, guest selectivity, and crystal density.[50,51] Therefore, the change of pore characteristics of **1-Et** may provide better application prospects for the adsorption, separation, optics, thermal stability, and chemical reaction activity.[53] The **1-Oct** shows type-II adsorption–desorption isotherm (Fig. S22†). It is not adsorptive for N_2 at 77 K, which is possibly due to the strong interactions between N_2 and the channel preventing N_2 diffusion into the **1-Oct** and/or the low kinetic energy of N_2, as shown in other MOFs.[54–57]

Published on 29 Desemba 2023. Downloaded on 24/08/2025 07:02:05.

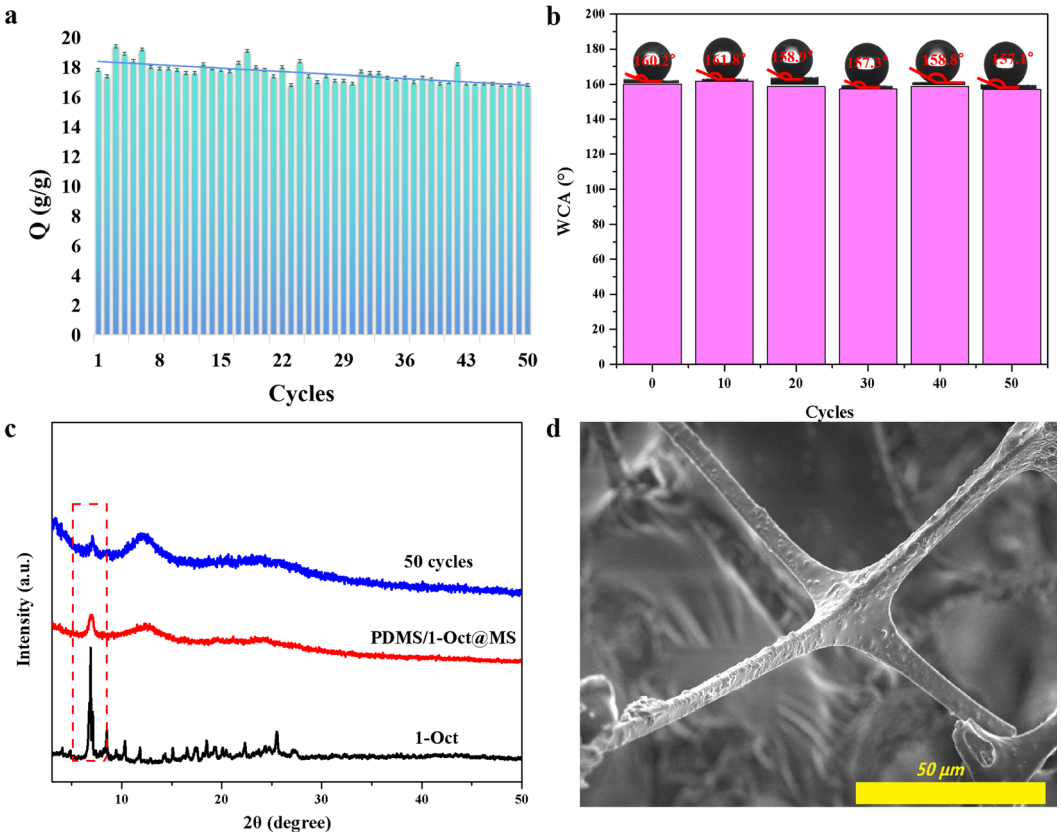

Fig. 8 Absorption capacity (a), WCAs (b), PXRD patterns (c), and SEM image (d) of PDMS/**1-Oct**@MS after 50 absorption cycles.

Conclusions

In summary, a 'bottom-up' strategy was adopted to introduce low-surface-energy alkyl chains into the H_2L ligand, and then a series of hydrophobic **1-R**s and **2-R**s were obtained through the coordination self-assembly engineering. The hydrophobicity of **1-R**s is enhanced by the introduction of alkyl chains with different lengths and even obtains superhydrophobic **1-Oct** with the WCAs increasing to 155.0°. The regular arrangement of alkyl chains strengthens the shielding effect on metal nodes and carboxylate groups leading to the enhancement of hydrophobicity. Moreover, the participation of alkyl chains also increases the roughness of **1-R**s in improving hydrophobicity. We then loaded superhydrophobic **1-Oct** onto MS by PDMS to obtain superhydrophobic PDMS/**1-Oct**@MS. The superposition effect of **1-Oct** and PDMS is more conducive to enhancing the hydrophobicity. PDMS/**1-Oct**@MS could efficiently and highly selectively separate oil–water, including the hard-separated water-in-oil emulsions. When PDMS/**1-Oct**@MS was applied to the simulated sea surface, an ideal effect of oil–water separation was still maintained. Remarkably, the performance was well maintained after 50 times absorption cycles.

Interestingly, unlike most reports, the introduction of *n*-butyl, *n*-hexyl, and *n*-octyl will lead to structural change. When the organic side chain is *n*-octyl, the crystal changes to 2D structure, and the π–π stacking between layers is also beneficial to the enhancement of hydrophobicity. However, it was a pity that the crystal structures were not obtained when the organic side chains were *n*-butyl and *n*-hexyl. After introducing ethyl, the PXRD patterns show that **1** and **1-Et** are isomorphic, but the N_2 adsorption–desorption isotherm changes from type-II to type-I isotherm. It may be that the introduction of ethyl results in a decrease in interpenetration. This work realized the transformation of MOF from 3D to 2D structure by introducing alkyl chains. At the same time, it could accurately regulate the hydrophobicity of MOFs and even realize the construction of superhydrophobic MOFs. The appropriate length of the alkyl chain could also improve the pore environment of interpenetrating MOF. It provides a promising strategy for constructing multi-functional superhydrophobic MOFs and the regulation of the pore environment.

Experimental section

Materials

All reagents and solvents used in this work are commercially available and used without further purification. Elemental analyses were performed with a Vario EL Cube elemental analyzer. The IR spectra were recorded (400–4000 cm^{-1} region) on a Thermo Scientific NICOLET 380 FT-IR. TG was carried out in an air atmosphere with a heating rate of 10 °C min^{-1} on a Mettler

 This journal is © the Partner Organisations 2024

Published on 29 Desemba 2023. Downloaded on 24/08/2025 07:02:05.

Toledo TG/DSC 3+. Powder X-ray diffraction (PXRD) data were collected on an Ultima IV automated multipurpose X-ray diffractometer using Cu-Kα radiation. The NMR experiments were carried out on Bruker AV-400 (400 MHz) or JEOL-500 (500 MHz) spectrometers. The N_2 adsorption isotherms were recorded at 77 K by using a Quantachrome EVO surface area and porosity analyzer. Before the adsorption measurement, the samples were activated at 100 °C under vacuum for 8 h. The surface morphologies and element distribution analyses were performed on a Regulus8230 Scanning Electron Microscope (SEM) with an Energy Dispersive Spectrometer (EDS). Before testing, the sample is sprayed with a thin layer of gold in a vacuum. The water contact angle (WCA) images were recorded by contact angle measuring device (SINDIN SDC-200s) with a high-speed camera of Dahang.

Synthesis of single crystal 1 ($[Cd(CuL^s)(L)]_n$)

A mixture of $Cd(NO_3)_2{\cdot}4H_2O$ (15.4 mg, 0.05 mmol) and CuL^s (19.5 mg, 0.03 mmol), H_2L (7.3 mg, 0.03 mmol) was dissolved in a mixed solvent of *N*,*N*-dimethylacetamide (DMA) and H_2O (DMA/H_2O, 5.0 mL/1.0 mL) in a 10 mL glass bottle with lid and heated at 90 °C for 4 days. After cooling to room temperature, dark block crystals were collected, washed with DMA and MeOH, and dried at 80 °C. Yield: 22.8 mg (75.8%). Elemental analysis data calculated (calcd) for $C_{52}H_{50}CdCuN_4O_6$: C, 62.22; H, 4.99; O, 9.57; N, 5.58%. Found: C, 61.18; H, 5.65; O, 10.88, N, 5.65%. The CCDC number for **1** is 2261019.

Synthesis of 1-Rs

A mixture of $Cd(NO_3)_2{\cdot}4H_2O$ (15.4 mg, 0.05 mmol), CuL^s (19.5 mg, 0.03 mmol), H_2L–Rs (Rs = NH_2, O–ethyl, O–*n*-butyl, O–*n*-hexyl, or O–*n*-octyl) were dissolved in a mixed solvent of DMA and H_2O (5.0 mL/1.0 mL) in a 10 mL glass bottle with lid and heated at 90 °C for 4 days. After cooling to room temperature, dark block crystals were collected, washed with DMA and MeOH, and dried at 80 °C. The CCDC number for **1-Oct** is 2313337.

Synthesis of single crystal 2 ($[Zn(CuL^s)(L)DMF]_n$)

A mixture of $Zn(NO_3)_2{\cdot}6H_2O$ (15.0 mg, 0.05 mmol) and CuL^s (19.5 mg, 0.03 mmol), H_2L (7.3 mg, 0.03 mmol) was dissolved in a mixed solvent of *N*,*N*-dimethylformamide (DMF) and H_2O (DMF/H_2O, 4.5 mL/0.5 mL) in a 10 mL glass bottle with lid and heated at 90 °C for 4 days. After cooling to room temperature, dark block crystals were collected, washed with DMF and MeOH, and dried at 80 °C. Yield: 21.5 mg (70.8%). Elemental analysis data calculated (calcd) for $C_{52}H_{50}CdCuN_4O_6$: C, 64.21; H, 5.45; O, 10.90; N, 6.81%. Found: C, 62.62; H, 3.77; O, 13.4; N, 6.80%. The CCDC number for **2** is 2234616.

Synthesis of 2-Rs

A mixture of $Zn(NO_3)_2{\cdot}6H_2O$ (15.0 mg, 0.05 mmol), CuL^s (19.5 mg, 0.03 mmol), H_2L–Rs (0.03 mmol) was dissolved in a mixed solvent of DMF and H_2O (4.5 mL/0.5 mL) in a 10 mL glass bottle with lid and heated at 90 °C for 4 days. After cooling to room temperature, dark block crystals were collected, washed with DMF and MeOH, and dried at 80 °C.

Preparation of PDMS/1-Oct@MS

The PDMS/**1-Oct**@MS composite sponge was prepared by immersing commercial MS into a mixture solution of **1-Oct** and PDMS. Specifically, the MS (1 × 1 × 1 cm^3) was ultrasonically cleaned with deionized water and absolute ethyl alcohol three times, 30 min each, and then dried to get clean MS. Then 1.0 g PDMS (with 0.1 g matching curing agent) and 0.1 g **1-Oct** were dispersed in 10 mL *n*-hexane and stirred for 30 min. Clean MS was immersed in the PDMS/**1-Oct** mixture solution in an ultrasonic bath for 20 min. Finally, the PDMS/**1-Oct**@MS was obtained after drying at 90 °C overnight. PDMS/MS and **1-Oct**@MS were also prepared by a similar method.

Oil–water separation tests

Layered oil separation tests. Herein, isopropanol, petroleum ether, ethyl alcohol, cyclohexane, ethyl acetate, toluene, dichloromethane, pump oil, hexane, and edible oil were used as models in the oil absorption tests. The absorption capacity (Q, g g^{-1}) of oil was calculated (eqn (1)) by measuring the mass of PDMS/**1-Oct**@MS before and after oil absorption.[4] In this work, methylene blue and Sudan III were used as water-soluble and fat-soluble dyes, respectively. PDMS/**1-Oct**@MS was immersed into the oil for 5 s, then took it out, and kept it in the air for 5 s so that the oil was no longer dripping, and finally weighed it. The separation efficiency and flux value were calculated according to eqn (2) and (3).[45]

$$Q = (m_1 - m_0)\ m_0^{-1} \quad (1)$$

Among them, Q is the absorption capacity, and m_0 and m_1 are the mass of PDMS/**1-Oct**@MS before and after saturated oil absorption, respectively.

$$\text{Separation efficiency } (\%) = m_1\ m_0^{-1} \quad (2)$$

Among them, m_0 and m_1 are the mass of dichloromethane before and after the separation process.

$$J = V\ A^{-1}\ t^{-1} \quad (3)$$

Among them, J is the flux, V (L) is the volume of the dichloromethane, A (m^2) is the effective PDMS/**1-Oct**@MS area, and t (h) is the separation time.

Emulsion separation experiment. The used water-in-oil emulsion was prepared by ultrasonic mixing of the dichloromethane and water mixture ($V_{Oil} : V_{H_2O}$ = 50 : 1) and emulsifier (span80, 0.02 mL mL^{-1}). Fix the sponge in the funnel and separate the dichloromethane by gravity. The separation efficiency and flux value were calculated also according to eqn (2) and (3).

Author contributions

X. H. and C. Y. are co-first authors. X. H., C. Y., and K.-Y. Y. conceptualized the study. X. H., C. Y., J. L., and Z. W. contributed to the synthesis. X. H. and C. Y. performed investigations. X. H. wrote the original draft. X. H., C. Y., and

Published on 29 Desemba 2023. Downloaded on 24/08/2025 07:02:05.

K.-Y. Y. reviewed and edited the final manuscript. All authors approved the final version of the manuscript.

Conflicts of interest

The authors declare no conflict of interest.

Acknowledgements

Financial support from the National Natural Science Foundation of China (22171046), the Hundred-Talent Project of Fujian (50021113), and Fuzhou University (510841) is gratefully acknowledged. Shiyanjia Lab (**https://www.shiyanjia.com**) provides technical support and assistance with the BET analysis.

References

1 Z. Chu, Y. Feng and S. Seeger, Oil/water separation with selective superantiwetting/superwetting surface materials, *Angew. Chem., Int. Ed.*, 2015, **54**, 2328–2338.
2 W. Zheng, J. Huang, S. Li, M. Ge, L. Teng, Z. Chen and Y. Lai, Advanced materials with special wettability toward intelligent oily wastewater remediation, *ACS Appl. Mater. Interfaces*, 2021, **13**, 67–87.
3 Z. Xue, Y. Cao, N. Liu, L. Feng and L. Jiang, Special wettable materials for oil/water separation, *J. Mater. Chem. A*, 2014, **2**, 2445–2460.
4 J. Chen, M. Sun, Y. Ni, T. Zhu, J. Huang, X. Li and Y. Lai, Superhydrophobic polyurethane sponge for efficient water-oil emulsion separation and rapid solar-assisted highly viscous crude oil adsorption and recovery, *J. Hazard. Mater.*, 2023, **445**, 130541.
5 M. Tao, L. Xue, F. Liu and L. Jiang, An intelligent superwetting PVDF membrane showing switchable transport performance for oil/water separation, *Adv. Mater.*, 2014, **26**, 2943–2948.
6 T. Sun, S. Hao, R. Fan, M. Qin, W. Chen, P. Wang and Y. Yang, Hydrophobicity-adjustable MOF constructs superhydrophobic MOF-rGO aerogel for efficient oil–water separation, *ACS Appl. Mater. Interfaces*, 2020, **12**, 56435–56444.
7 B.-H. Li, S.-L. Wang, S. Pal, P. B. So, G.-Y. Chen, W.-J. Huang, Y.-L. Hsu, S.-Y. Kuo, J.-M. Yeh and C.-H. Lin, Versatile reactions on hydrophobic functionalization of metal-organic frameworks and anticorrosion application, *Microporous Mesoporous Mater.*, 2021, **325**, 111319.
8 K. Jayaramulu, F. Geyer, A. Schneemann, Š. Kment, M. Otyepka, R. Zboril, D. Vollmer and R. A. Fischer, Hydrophobic metal–organic frameworks, *Adv. Mater.*, 2019, **31**, 1900820.
9 X. Zhang, Z. Chen, X. Liu, S. L. Hanna, X. Wang, R. Taheri-Ledari, A. Maleki, P. Li and O. K. Farha, A historical overview of the activation and porosity of metal–organic frameworks, *Chem. Soc. Rev.*, 2020, **49**, 7406–7427.
10 S. Natarajan and P. Mahata, Metal–organic framework structures–how closely are they related to classical inorganic structures?, *Chem. Soc. Rev.*, 2009, **38**, 2304–2318.
11 L. Hashemi, M. Y. Masoomi and H. Garcia, Regeneration and reconstruction of metal-organic frameworks: Opportunities for industrial usage, *Coord. Chem. Rev.*, 2022, **472**, 214776.
12 A. J. Howarth, A. W. Peters, N. A. Vermeulen, T. C. Wang, J. T. Hupp and O. K. Farha, Best practices for the synthesis, activation, and characterization of metal–organic frameworks, *Chem. Mater.*, 2017, **29**, 26–39.
13 H.-L. Jiang, T. A. Makal and H.-C. Zhou, Interpenetration control in metal–organic frameworks for functional applications, *Coord. Chem. Rev.*, 2013, **257**, 2232–2249.
14 S. Yuan, L. Feng, K. Wang, J. Pang, M. Bosch, C. Lollar, Y. Sun, J. Qin, X. Yang, P. Zhang, Q. Wang, L. Zou, Y. Zhang, L. Zhang, Y. Fang, J. Li and H.-C. Zhou, Stable metal–organic frameworks: design, synthesis, and applications, *Adv. Mater.*, 2018, **30**, 1704303.
15 X. Liu, P. Zhang, H. Xiong, Y. Zhang, K. Wu, J. Liu, R. Krishna, J. Chen, S. Chen, Z. Zeng, S. Deng and J. Wang, Engineering pore environments of sulfate-pillared metal-organic framework for efficient C_2H_2/CO_2 separation with record selectivity, *Adv. Mater.*, 2023, **35**, 2210415.
16 J. Wang, Y. Zhang, Y. Su, X. Liu, P. Zhang, R. Lin, S. Chen, Q. Deng, Z. Zeng, S. Deng and B. Chen, Fine pore engineering in a series of isoreticular metal-organic frameworks for efficient C_2H_2/CO_2 separation, *Nat. Commun.*, 2022, **13**, 200.
17 Y. Wang, H. Li, X. He and Z. Xu, Application in anticounterfeiting for multistimuli smart luminescent materials based on MOF-on-MOF, *Inorg. Chem.*, 2021, **60**, 15001–15009.
18 C. Pettinari, R. Pettinari, C. Di Nicola, A. Tombesi, S. Scuri and F. Marchetti, Antimicrobial MOFs, *Coord. Chem. Rev.*, 2021, **446**, 214121.
19 N. Hanikel, M. S. Prévot and O. M. Yaghi, MOF water harvesters, *Nat. Nanotechnol.*, 2020, **15**, 348–355.
20 R. Freund, O. Zaremba, G. Arnauts, R. Ameloot, G. Skorupskii, M. Dincă, A. Bavykina, J. Gascon, A. Ejsmont, J. Goscianska, M. Kalmutzki, U. Lächelt, E. Ploetz, C. S. Diercks and S. Wuttke, The current status of MOF and COF applications, *Angew. Chem., Int. Ed.*, 2021, **60**, 23975–24001.
21 H. Yuan, N. Li, W. Fan, H. Cai and D. Zhao, Metal-organic framework based gas sensors, *Adv. Sci.*, 2022, **9**, 2104374.
22 S. Mallakpour, E. Nikkhoo and C. M. Hussain, Application of MOF materials as drug delivery systems for cancer therapy and dermal treatment, *Coord. Chem. Rev.*, 2022, **451**, 214262.
23 A. Bavykina, N. Kolobov, I. S. Khan, J. A. Bau, A. Ramirez and J. Gascon, Metal–organic frameworks in heterogeneous catalysis: recent progress, new trends, and future perspectives, *Chem. Rev.*, 2020, **120**, 8468–8535.
24 R. M. Rego, G. Kuriya, M. D. Kurkuri and M. Kigga, MOF based engineered materials in water remediation: Recent trends, *J. Hazard. Mater.*, 2021, **403**, 123605.

 This journal is © the Partner Organisations 2024

Published on 29 Desemba 2023. Downloaded on 24/08/2025 07:02:05.

25 K. Jayaramulu, F. Geyer, A. Schneemann, Š. Kment, M. Otyepka, R. Zboril, D. Vollmer and R. A. Fischer, Hydrophobic metal–organic frameworks, *Adv. Mater.*, 2019, **31**, 1900820.
26 C. Liu, Q. Liu and A. Huang, A superhydrophobic zeolitic imidazolate framework (ZIF-90) with high steam stability for efficient recovery of bioalcohols, *Chem. Commun.*, 2016, **52**, 3400–3402.
27 N.-X. Zhu, Z.-W. Wei, C.-X. Chen, D. Wang, C.-C. Cao, Q.-F. Qiu, J.-J. Jiang, H.-P. Wang and C.-Y. Su, Self-generation of surface roughness by low-surface-energy alkyl chains for highly stable superhydrophobic/superoleophilic MOFs with multiple functionalities, *Angew. Chem., Int. Ed.*, 2019, **58**, 17033–17040.
28 Z. Xu, J. Wang, H. Li and Y. Wang, Coating sponge with multifunctional and porous metal-organic framework for oil spill remediation, *Chem. Eng. J.*, 2019, **370**, 1181–1187.
29 S. Ghosh, A. Rana, S. Kumar, C. Gogoi, S. Mukherjee, U. Manna and S. Biswas, A self-cleaning hydrophobic MOF-based composite for highly efficient and recyclable separation of oil from water and emulsions, *Mater. Chem. Front.*, 2022, **6**, 2051–2060.
30 F. J. Uribe-Romo, J. R. Hunt, H. Furukawa, C. Klöck, M. O'Keeffe and O. M. Yaghi, A crystalline imine-linked 3D porous covalent organic framework, *J. Am. Chem. Soc.*, 2009, **131**, 4570–4571.
31 T. Ma, J. Li, J. Niu, L. Zhang, A. S. Etman, C. Lin, D. Shi, P. Chen, L.-H. Li, X. Du, J. Sun and W. Wang, Observation of interpenetration isomerism in covalent organic frameworks, *J. Am. Chem. Soc.*, 2018, **140**, 6763–6766.
32 A. L. Spek, Single-crystal structure validation with the program PLATON, *J. Appl. Crystallogr.*, 2003, **36**, 7–13.
33 G. Hai, X. Jia, K. Zhang, X. Liu, Z. Wu and G. Wang, High-performance oxygen evolution catalyst using two-dimensional ultrathin metal-organic frameworks nanosheets, *Nano Energy*, 2018, **44**, 345–352.
34 X. He, H. Li, J. Wang, Y. Li, M. Su and Z. Xu, Tunable dual-mode MOF-based composite fluorescent materials: Stimuli-responsive and anti-counterfeiting application, *Cryst. Growth Des.*, 2021, **21**, 1625–1635.
35 S. Barthwal, Y. Jeon and S. Lim, Superhydrophobic sponge decorated with hydrophobic MOF-5 nanocoating for efficient oil-water separation and antibacterial applications, *Sustainable Mater. Technol.*, 2022, **33**, e00492.
36 J. Saleem, M. A. Riaz and M. Gordon, Oil sorbents from plastic wastes and polymers: A review, *J. Hazard. Mater.*, 2018, **341**, 424–437.
37 C. Gogoi, A. Rana, S. Ghosh, R. Fopase, L. M. Pandey and S. Biswas, Superhydrophobic self-cleaning composite of a metal–organic framework with polypropylene fabric for efficient removal of oils from oil–water mixtures and emulsions, *ACS Appl. Nano Mater.*, 2022, **5**, 10003–10014.
38 W. Xiang, H. Liu, J. Zhu, H. Gong and Q. Cao, Room temperature hydroxyl group-assisted preparation of hydrophobicity-adjustable metal-organic framework UiO-66 composites: Towards continuous oil collection and emulsion separation, *Chem. – Eur. J.*, 2023, **29**, e202300662.
39 H. Saini, P. Kallem, E. Otyepková, F. Geyer, A. Schneemann, V. Ranc, F. Banat, R. Zbořil, M. Otyepka, R. A. Fischer and K. Jayaramulu, Two-dimensional MOF-based liquid marbles: surface energy calculations and efficient oil–water separation using a ZIF-9-III@PVDF membrane, *J. Mater. Chem. A*, 2021, **9**, 23651–23659.
40 J. Gu, H. Fan, C. Li, J. Caro and H. Meng, Robust superhydrophobic/superoleophilic wrinkled microspherical MOF@rGO composites for efficient oil–water separation, *Angew. Chem., Int. Ed.*, 2019, **58**, 5297–5301.
41 A. Rana, S. Ghosh and S. Biswas, An eco-friendly approach using a nonfluorous self-cleaning metal–organic framework composite and membrane for oil–water separation, *Inorg. Chem. Front.*, 2023, **10**, 612–620.
42 L. Feng, S.-H. Lo, K. Tan, B.-H. Li, S. Yuan, Y.-F. Lin, C.-H. Lin, S.-L. Wang, K.-L. Lu and H.-C. Zhou, An encapsulation-rearrangement strategy to integrate superhydrophobicity into mesoporous metal-organic frameworks, *Matter*, 2020, **2**, 988–999.
43 R. Dalapati, S. Nandi, C. Gogoi, A. Shome and S. Biswas, Metal–organic framework (MOF) derived recyclable, superhydrophobic composite of cotton fabrics for the facile removal of oil spills, *ACS Appl. Mater. Interfaces*, 2021, **13**, 8563–8573.
44 O. Duman, C. Ö. Diker and S. Tunç, Development of highly hydrophobic and superoleophilic fluoro organothiol-coated carbonized melamine sponge/rGO composite absorbent material for the efficient and selective absorption of oily substances from aqueous environments, *J. Environ. Chem. Eng.*, 2021, **9**, 105093.
45 O. Duman, C. Ö. Diker, H. Uğurlu and S. Tunç, Highly hydrophobic and superoleophilic agar/PVA aerogels for selective removal of oily substances from water, *Carbohydr. Polym.*, 2022, **286**, 119275.
46 O. Duman, C. Ö. Diker, S. M. Güreşir, U. Cengiz and S. Tunç, Superhydrophobic melamine sponge-sorbent fabricated using WS_2, halloysite nanotube, octyltriethoxysilane, tetraethoxysilane, and polydimethylsiloxane for the selective uptake of oil from water, *J. Water Process Eng.*, 2023, **56**, 104454.
47 D. Lang, G. Liu, R. Wu, G. Chen, C. Zhang, C. Yang, W. Wang, J. Wang and J. Fu, One-step preparation of robust elastic plastic polyvinyl chloride sponges with a layered structure for highly efficient separation of water-in-oil emulsions, *Chem. Eng. J.*, 2023, **471**, 144752.
48 G. Zhai, J. Wu, Z. Yuan, H. Li and D. Sun, Robust superhydrophobic PDMS@SiO_2@UIO66-OSiR sponge for efficient water-in-oil emulsion separation, *Inorg. Chem.*, 2023, **62**, 5447–5457.
49 L. Han, H. Bi, X. Xie, S. Su, P. Mao and L. Sun, Superhydrophobic graphene-coated sponge with microcavities for high efficiency oil-in-water emulsion separation, *Nanoscale*, 2020, **12**, 11782–17812.

50 H.-L. Jiang, T. A. Makal and H.-C. Zhou, Interpenetration control in metal–organic frameworks for functional applications, *Coord. Chem. Rev.*, 2013, **257**, 2232–2249.
51 M. Gupta and J. J. Vittal, Control of interpenetration and structural transformations in the interpenetrated MOFs, *Coord. Chem. Rev.*, 2021, **435**, 213789.
52 M. I. Nandasiri, S. R. Jambovane, B. P. McGrail and H. T. Schaef, Adsorption, separation, and catalytic properties of densified metal-organic frameworks, *Coord. Chem. Rev.*, 2016, **311**, 38–52.
53 G. Verma, S. Butikofer, S. Kumar and S. Ma, Regulation of the degree of interpenetration in metal–organic frameworks, *Top. Curr. Chem.*, 2020, **378**, 4.
54 P. S. Nugent, V. L. Rhodus, T. Pham, K. Forrest, L. Wojtas, B. Space and M. J. Zaworotko, A robust molecular porous material with high CO_2 uptake and selectivity, *J. Am. Chem. Soc.*, 2013, **135**, 10950–10953.
55 S. Yang, L. Zhou, Y. He, R. Krishna, Q. Zhang, Y. An, B. Xing, Y. Zhang and T. Hu, Two-dimensional metal–organic framework with ultrahigh water stability for separation of acetylene from carbon dioxide and ethylene, *ACS Appl. Mater. Interfaces*, 2022, **14**, 33429–33437.
56 W. Shi, Y. Li, J. Chen, R. Su, L. Hou, Y. Wang and Z. Zhu, A new metal–organic framework based on rare $[Zn_4F_4]$ cores for efficient separation of C_2H_2, *Chem. Commun.*, 2021, **57**, 12788–12791.
57 A. Hazra, S. Bonakala, S. A. Adalikwu, S. Balasubramanian and T. K. Maji, Fluorocarbon-functionalized superhydrophobic metal–organic framework: enhanced CO_2 uptake via photoinduced postsynthetic modification, *Inorg. Chem.*, 2021, **60**, 3823–3833.

Published on 29 Desemba 2023. Downloaded on 24/08/2025 07:02:05.

This journal is © the Partner Organisations 2024